

This is the accepted manuscript made available via CHORUS. The article has been published as:

Copper-substituted iron telluride: A phase diagram

Patrick N. Valdivia, Min Gyu Kim, Thomas R. Forrest, Zhijun Xu, Meng Wang, Hui Wu, Leland W. Harringer, Edith D. Bourret-Courchesne, and Robert J. Birgeneau

Phys. Rev. B **91**, 224424 — Published 22 June 2015

DOI: [10.1103/PhysRevB.91.224424](https://doi.org/10.1103/PhysRevB.91.224424)

Copper substituted iron telluride: a phase diagram

Revised 5/29/2015 15:39:00

Patrick N. Valdivia,¹ Min Gyu Kim,² Thomas R. Forrest,³ Zhijun Xu,³ Meng Wang,³ Hui Wu,^{4,5} Leland W. Harringer,⁴ Edith D. Bourret-Courchesne,² and Robert J. Birgeneau^{1,2,3}

¹University of California, Berkeley, Department of Materials Science, Berkeley CA 94720

²Lawrence Berkeley Laboratory, Materials Science Division, Berkeley CA 94720

³University of California, Berkeley, Department of Physics, Berkeley CA 94720

⁴NIST Center for Neutron Research, 100 Bureau Drive, Gaithersburg MD 20899

⁵University of Maryland, Department of Materials Science and Engineering, College Park MD 20742

We have studied the structure, magnetic, and transport properties of copper substituted iron telluride. Our results extend the range of copper substitution to 60% substitution per formula unit, which is far beyond previously stated solubility limits. Substitution of copper into antiferromagnetic iron telluride is found to suppress the signatures of the low-temperature transitions in susceptibility and resistance measurements, giving rise to an insulating, spin glass state. Upon increasing the copper substitution from 4% to 6%, short range antiferromagnetic order appears followed by the combined magnetic and structural transition at a lower temperature, although the magnetic order is ultimately not resolution limited with a correlation length of 250 Å in the 6% Cu-substituted sample, in contrast to the magnetic order of the 4% copper substituted sample, which is resolution limited. Upon warming the 6% Cu-substituted sample in the presence of a 5 T magnetic field oriented along the *b* axis, magnetic and structural phase transitions are observed at a temperature much lower than those of the magnetic and structural transitions which occur in zero field. Furthermore, these transitions are absent upon cooling in this field. We discuss the field results in the most general terms possible, including possible random field effects.

PACS: 74.70.Xa, 64.70.Rh, 75.30.Hx, 75.40.-s

1. INTRODUCTION

The nonstoichiometric $\text{Fe}_{1+\delta}\text{Te}^{1-9}$ and the transition metal substituted $\text{Fe}_{1+\delta-x}\text{TM}_x\text{Te}$ ($\text{TM} = \text{Ni}^{10}, \text{Cu}^{11-19}, \text{Pd}^{20}$) compounds exhibit intriguing interconnections between structure, magnetism, and electronic properties. The various forms of magnetism in $\text{Fe}_{1+\delta-x}\text{TM}_x\text{Te}$ appear at the antiferromagnetic wave vector $\mathbf{Q}_{\text{AFM}} = (0.5-\varepsilon, 0, L)$, which is different from the nesting vector², although the electron and hole pockets in the Fermi surface can be connected by a nesting vector¹. Therefore it has been argued that the antiferromagnetic (AFM) order in the family of $\text{Fe}_{1+\delta}\text{Te}$ compounds arises from localized electrons^{21,22}. In $\text{Fe}_{1+\delta}\text{Te}$ with $\delta \leq 0.09$, the low-temperature antiferromagnetic order is commensurate and forms a double stripe (also referred to as bicollinear) AFM structure with moments pointing along the longer *b* direction; perpendicular to the propagation vector $\mathbf{Q}_{\text{AFM}} = (0.5-\varepsilon, 0, 0.5)^2$. This bicollinear order is accompanied by a tetragonal-to-monoclinic structural transition². With more excess Fe ($0.09 < \delta < 0.14$), the low-temperature AFM ordering becomes incommensurate (the SDW phase in Rodriguez et. al²). This SDW phase can be either long-ranged as in $\text{Fe}_{1.09}\text{Te}$ or short-ranged as in $\text{Fe}_{1.12}\text{Te}$ where it coexists with long-range helical order². Finally, for $\delta \geq 0.14$ the magnetism develops a *c*-axis component of the moment, referred to as a helical order, and

the magnetic transition is accompanied by an orthorhombic structural transition². All of these structural and magnetic transitions occur below $T = 70$ K, and decrease in temperature with increasing δ , down to $T \approx 45$ K in $\text{Fe}_{1.14}\text{Te}^3$. Both the structural and AFM transitions are first order at $\delta \approx 0.11$ and second order transitions at higher δ , implying a multicritical point^{4,5}. A phase transition occurs initially from paramagnetic and tetragonal to incommensurate AFM in either the orthorhombic⁵ or monoclinic⁶ structure at compositions just above the critical point, then gives way to a transition towards nearly-commensurate order of the bicollinear structure^{2,4-6}. It is not clear whether these transitions occur in a single phase⁴ or in separate phases that interact^{2,5}.

In $\text{Fe}_{1+\delta-x}\text{TM}_x\text{Te}$ ($\text{TM} = \text{Ni}^{10}, \text{Cu}^{11,12}, \text{and Pd}^{20}$) compounds, as transition metal elements are introduced into the system, the structural and AFM transitions are also suppressed as in the $\text{Fe}_{1+\delta}\text{Te}$ compounds and it was found that a subtle difference in the substitution level produces various interesting structural and magnetic properties. In particular, for $\text{Fe}_{1.10}\text{Cu}_{0.04}\text{Te}$, a first-order magnetic transition occurs at $T = 37$ K and the AFM ordering is bicollinear at a nearly-commensurate wavevector $\mathbf{Q}_{\text{AFM}} = (0.494, 0, 0.5)^{12}$. In a compound with slightly more Cu content ($\text{Fe}_{1.04}\text{Cu}_{0.1}\text{Te}$), a short-range AFM ordering was observed at $\mathbf{Q}_{\text{AFM}} = (0.48, 0, 0.5)$ up to $T = 80$ K, and a spin-glass-like behavior was also observed in susceptibility at $T = 22$ K¹². The

incommensurability ε [defined by $(0.5-\varepsilon, 0, 0.5)$] observed for these copper substituted compounds is much smaller than that of the $\mathbf{Q}_{\text{AFM}} = (0.38, 0, 0.5)$ in $\text{Fe}_{1.12}\text{Te}$ and $\text{Fe}_{1.14}\text{Te}$ compounds^{2,7} or $\mathbf{Q}_{\text{AFM}} = (0.34, 0, 0.5)$ in $\text{Fe}_{1.17}\text{Te}$ ⁷. From these results, it seems that Cu substitution may drive the magnetic order from incommensurate SDW or helical towards the commensurate bicollinear AFM order. However, according to one model, the “semiconducting-like” transition in the low temperature resistance data¹¹ implies the helical magnetic structure in which the spin-gap is closed^{5,23} as in $\text{Fe}_{1+\delta}\text{Te}$ with $\delta \geq 0.14$. Therefore, it is not yet clear how Cu substitution affects the magnetic properties in this family.

Another puzzle in $\text{Fe}_{1+\delta-x}\text{Cu}_x\text{Te}$ is contrasting properties in similar compounds, especially at higher copper compositions. For example, nonstoichiometric $\text{Fe}_{0.66}\text{Cu}_{0.61}\text{Te}$ ¹⁵ and stoichiometric $\text{Fe}_{0.5}\text{Cu}_{0.5}\text{Te}$ ¹⁴ compounds exhibit spin density wave transitions (not necessarily of the same type as in Rodriguez et. al²) at $T = 256$ K and 308 K, respectively, although the crystal structures were not reported^{14,15}. Another group showed that in $\text{Fe}_{0.61}\text{Cu}_{0.565}\text{Te}$ a tetragonal structure (isostructural to $\text{Fe}_{1+\delta}\text{Te}$) exists down to $T = 4$ K while a spin glass transition occurs between $T = 70$ and 90 K¹³ whereas a third group also produced $\text{Fe}_{0.61}\text{Cu}_{0.565}\text{Te}$ and reported that their sample is paramagnetic at all temperatures above $T = 10$ K¹⁶. Despite these works at high copper substitution, it has also been reported that copper is not miscible in the $\text{Fe}_{1+\delta-x}\text{Cu}_x\text{Te}$ structure with $x \geq 0.2$ or 0.3¹².

The transport properties of $\text{Fe}_{1+\delta-x}\text{Cu}_x\text{Te}$ compounds are also intriguing. For instance, the resistance exhibits a change in behavior (a “metal-to-semiconductor” transition⁵) in $\text{Fe}_{1+\delta-x}\text{Cu}_x\text{Te}$ ¹¹. The metallic behavior was previously observed in $\text{Fe}_{1+\delta}\text{Te}$ with $\delta \approx 0.06$ ⁵ and associated with the existence of a spin gap^{5,23}. The spin gap is closed when the magnetic structure develops c -axis component of the moment and forms a helical order in $\delta \approx 0.14$ ^{5,23}. Alternatively, a DFT calculation suggests Anderson localization for the origin of the “metal-to-semiconductor” transition which occurs in $\text{Fe}_{1-x}\text{Cu}_x\text{Se}$ due to local electronic disorder introduced by filled d^{10} shells of copper²⁴. The variable range hopping model, which can signify Anderson localization²⁵ is successfully applied in $\text{Fe}_{1-x}\text{Cu}_x\text{Se}$ ²⁶, $\text{Fe}_{0.5}\text{Cu}_{0.5}\text{Te}$ ¹⁷ and $\text{Fe}_{0.98-x}\text{Cu}_x\text{Se}_{0.5}\text{Te}_{0.5}$ ²⁷, $z = 0.02$ and 0.1. However, other studies have suggested that $\text{Fe}_{0.5}\text{Cu}_{0.5}\text{Te}$ is a zero bandgap semiconductor, wherein the resistance scales as a power law in temperature^{16,18} reflecting intrinsic power law behaviors in the carrier concentration, and that the exponent’s value indicates diffusive transport due to formation of spin polarons^{16,28,29}.

To shed light on the complex physical properties in $\text{Fe}_{1+\delta-x}\text{Cu}_x\text{Te}$, we present synthesis of a series of single crystals of $\text{Fe}_{1+\delta-x}\text{Cu}_x\text{Te}$ compounds and their resistance and susceptibility. We also report the structural and antiferromagnetic properties in several compounds studied by x-ray powder diffraction, neutron powder diffraction and

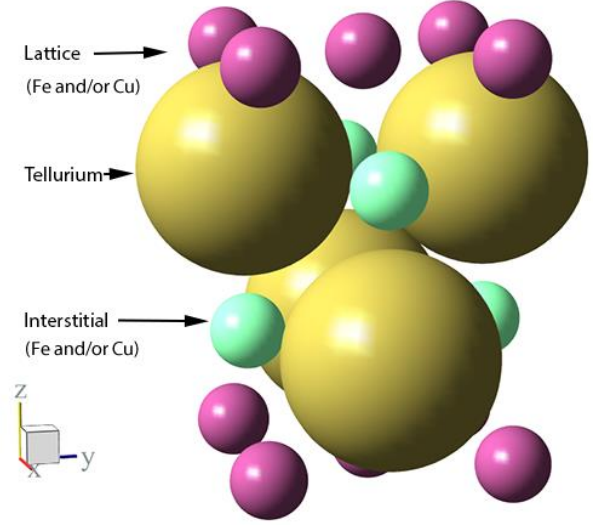


FIG. 1 The crystal structure (visualized in origin choice 1) of $\text{Fe}_{1+\delta-x}\text{Cu}_x\text{Te}$ compounds. The interstitial sites are only slightly occupied by the amount δ as described in the text. The interstitial metal and tellurium atoms are both situated on (2c) sites, which have a free parameter as the height from the metallic lattice plane.

neutron single crystal diffraction measurements. We find that copper can replace iron up to 60% per formula unit, which is far beyond previously assumed solubility limits¹² in the structure (Fig. 1). We show that the resistance data cannot be fit to the variable range hopping model at any composition while the zero bandgap model can fit our data for 52% and 57% Cu substitutions. Our neutron measurements show a single first order magneto-structural transition in 4% Cu substitution, and two separated structural and/or magnetic transitions in 6% Cu substitution. We demonstrate that the AFM ordering is long-ranged and commensurate in 4% Cu substitution and short-ranged incommensurate with a spin correlation length of 250 Å in 6% Cu substitution. We also find that upon applying an external magnetic field, additional structural and magnetic transitions appear at lower temperature. We discuss the nature of the transitions in field, which might result from random field effects.

2. EXPERIMENTAL METHODS

We synthesized $\text{Fe}_{1+\delta-x}\text{Cu}_x\text{Te}$ (FCT) single crystals using a modified Bridgman growth technique that utilizes the natural temperature gradient in horizontal, single zone tube furnaces. The furnaces were asymmetrically insulated, and the temperature gradient at the end of each of the furnaces where the initial solidification occurs is roughly 5 °C/cm when the furnaces are at a setpoint of 1000 °C. Pieces of elemental iron (4N), tellurium shot (4N), and pieces cut from copper sheet (8N), were combined in an Argon filled glovebox, and reacted in doubly-sealed quartz ampoules

using a two-step procedure. The first step was a pre-melting reaction intended to homogenize the reactants following that previously used to synthesize other iron-chalcogenides³⁰. The reacted material was then brought back into the glovebox, where the quartz was broken and the material was ground into a fine powder and loaded into clean quartz ampoules. The second step used a higher melting temperature than that used in the previous studies^{12,30} in order to ensure homogeneity of the melt³¹. After heating to 625 °C at a rate of 0.5 °C/min and holding for 12 hours, then heating to 975 °C at 0.5 °C/min and holding for 30 hours, the tubes were heated to 1075 °C at a rate of 0.5 °C/min and held for 30 hours. Then the tubes were cooled first to 650 °C (3 °C/hr) followed by 415 °C (0.5 °C/min), held for 24 hours, and finally cooled to room temperature at a rate of 0.5 °C/min.

The synthesis resulted in large single crystalline boules at all compositions studied, except in the sample of nominal copper free composition $\text{Fe}_{1.08}\text{Te}$, which appears noncrystalline and produced a multiphase product as observed by x-ray powder diffraction. Crystals extracted from the boules had a reflective silver luster, in contrast with the gold color reported at $x \approx 0.5$ in some previous studies^{18,19}. All crystals became less lustrous if left in air at room temperature over the time scale of several weeks; however, the samples were always stored in a glovebox until it became necessary to remove them for measurements.

For elemental analysis, Energy Dispersive X-ray Spectroscopy (EDX) was performed on the *ab*-plane of single crystal samples using a Leo 430 Scanning Electron Microscope. Measurements were performed with over 50,000 points collected over an area of at least 0.1 mm². The compositions were extracted by integrating the Cu-K α , Cu-K β , Fe-K α , Fe-K β , Te-L α , Te-L β , and Te-L γ peak profiles across the entire scanned area. From these ratios we obtained $x_{\text{EDX}} = \text{Cu}/\text{Te}$ and $\delta_{\text{EDX}} = (\text{Cu} + \text{Fe})/\text{Te} - 1$. Three samples were measured from each growth batch, and when the nominal concentration of copper $x_{\text{nom}} \geq 0.3$, six samples were measured, as further explained in the results section. The errors in the values x_{EDX} and δ_{EDX} , estimated by the counting statistics of each measurement, were less than 1% for all compounds.

Powder diffraction data were collected at room temperature with a PANalytical X'Pert Pro diffractometer using Co-K α_1 radiation. The lattice parameters were obtained by refinement using LaB₆ (NIST SRM 660b) as a positional calibrant.

For structural refinement beyond the lattice parameters, and for an additional check of the phase purity, neutron powder diffraction (NPD) measurements were performed on two samples with the BT-1 diffractometer at the NIST Center for Neutron Research. The refinements of the crystal structures were performed with GSAS+EXPGUI³².

Susceptibility measurements were primarily performed using a Quantum Design Physical Properties Measurement System (PPMS), while a Magnetic Properties Measurement

System (MPMS) was used to check cooling/warming hysteresis of the AFM transitions of the samples with $x_{\text{EDX}} \leq 0.06$. Both zero-field-cooled and field-cooled measurements were performed between 2 K and 350 K. Low field measurements were obtained in a field of $\mu_0 H = 0.1$ T and high field measurements were obtained at 5 T. In each case the field was aligned parallel to the *ab*-plane. For the PPMS measurements, cooling from high temperature was performed in a two-step process involving 2 hours dwell time upon cooling to 50 K and to 2 K, in order to ensure a uniform temperature environment for the measurement.

In order to determine the low-temperature magnetic and structural properties of $x_{\text{EDX}} = 0.04$ and $x_{\text{EDX}} = 0.06$ compounds, elastic neutron diffraction was performed on single crystals of these compositions at the NG-5 triple axis beamline (SPINS) at the NIST Center for Neutron Research, using $\lambda = 4.09$ Å neutrons. A cooled beryllium filter was used to remove the $\lambda/2$ harmonic. The masses of these samples were 0.498 g for $x_{\text{EDX}} = 0.04$ and 0.488 g for $x_{\text{EDX}} = 0.06$. Measurements for the $x_{\text{EDX}} = 0.04$ sample were performed in a sample can which was loaded into a closed cycle refrigerator, and measurements were taken between 6.5 and 70 K. For the $x_{\text{EDX}} = 0.06$ sample, the sample was loaded into a displex/cryostat and all of the measurements, including those in zero field, were performed with a 7 T vertical field magnet installed, which reduced the incident neutron intensity by a factor of roughly ten; measurements in this environment were taken between 2 K and 80 K.

Resistance measurements were also performed with a Quantum Design PPMS. As silver paint contacts often fail for the iron-chalcogenides³³, low-resistance contacts were fabricated by sputtering 500 Å Ti/8000 Å Au pads on the sample and gold wires were bonded to the contacts using silver paint. The measurements were performed between 2 and 300 K.

3. RESULTS AND DISCUSSION

A. Stoichiometry

Figure 2a shows the relation between the actual Cu concentration (x_{EDX}) and the starting (nominal) concentration (x_{nom}) for each growth batch of $\text{Fe}_{1+\delta-x}\text{Cu}_x\text{Te}$, with separate labels for growth batches which were initially distinguished by different nominal iron content: $\delta_{\text{nom}} = 0.08$ and 0.18. When $x_{\text{nom}} \leq 0.2$, the actual concentration tracks the nominal concentration for individual pieces and for the average, while for concentrations of $x_{\text{nom}} \geq 0.3$, a range of concentrations was produced with a standard deviation of $\sigma(x_{\text{EDX}}) \approx 0.1$ for each growth batch; furthermore x_{EDX} is much greater than x_{nom} in the three growth batches which ended up having the highest actual compositions. Thus we measured an additional three samples for each growth batch with $x_{\text{nom}} \geq 0.3$ to investigate the homogeneity of the boules along their length, but did not observe any consistent segregation characteristic. We also measured six samples

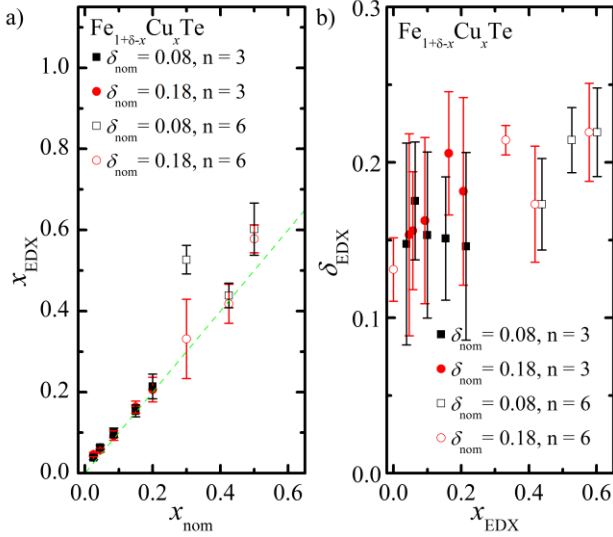


FIG. 2 EDX-mapping data measured for the different growth batches. Average concentrations are determined with three randomly selected pieces of crystal ($n = 3$) for nominal concentration $x_{\text{nom}} \leq 0.2$, and six pieces of crystal ($n = 6$) for $x_{\text{nom}} \geq 0.3$. a) Average EDX copper concentration $x_{\text{EDX}} = \text{Cu}/\text{Te}$ as a function of x_{nom} . b) Average excess metal ratio $\delta_{\text{EDX}} = [(\text{Cu} + \text{Fe})/\text{Te}] - 1$ versus average copper concentrations x_{EDX} . Error bars indicate the standard deviation of the two sets of growth batches at low x_{nom} and single growth batches at high x_{nom} , so that the number of samples in each set is 6. The dashed green line represents the line of nominal composition.

for $\delta = 0.18$, $x_{\text{EDX}} = 0$ as the $\delta = 0.08$ product was multiphase. Within the samples with $x_{\text{nom}} \geq 0.3$, the EDX-measured compositions were consistent across the samples which were ~ 10 millimeters wide, and when comparing the front and back surfaces of samples 2 to 3 millimeters thick. However, since a spread of compositions exists within the boules for $x_{\text{nom}} \geq 0.3$, the actual compositions (x_{EDX}) were measured on the same crystals for which we measured powder diffraction, susceptibility, and resistance for these samples (when $x_{\text{nom}} \geq 0.3$). Therefore, we will use the variable x_{EDX} throughout the paper to denote the average of all EDX measurements when $x_{\text{nom}} \leq 0.2$ and for the concentration of the piece of crystal measured in the physical property measurement specified when $x_{\text{nom}} \geq 0.3$, except in this section (correspondingly, Fig. 2) and in the section on neutron powder diffraction measurements (Fig. 3) where it represents the average of all samples measured.

Figure 2b shows a plot of the averaged δ_{EDX} vs. x_{EDX} for each growth batch. A positive correlation between δ_{EDX} and x_{EDX} is evident. This can be interpreted in at least three ways: (i) the total amount of metal in the phase increases with copper substitution (ii) the occupancy of the tellurium site decreases with copper substitution or (iii) additional impurity phases with a higher $(\text{Fe} + \text{Cu})/\text{Te}$ ratio are formed at high copper substitution; any combination of the above

cases may also occur. We shall show evidence in the neutron powder diffraction section that the first mechanism (i) likely does not contribute to this trend. Comparing the low-temperature resistive properties observed in our copper-free samples of $\text{Fe}_{1+\delta}\text{Te}$ with previous reports⁵ it is highly likely that $\delta \leq 0.11$; using reference data obtained for magnetic susceptibility of crystals with various composition in $\text{Fe}_{1+\delta}\text{Te}$, we believe that we have obtained $\text{Fe}_{1.07}\text{Te}$ ³, whereas our EDX results give $\delta_{\text{EDX}} = 0.13$. In general, we did not observe surface oxides or other impurity phases on the sample surfaces by EDX, and there were only subtle deviations of the measured composition at crystal edges and facets. We shall discuss evidences of slight amounts of impurity phases in the results of susceptibility measurements and in the section on neutron powder diffraction. For the EDX measurements, we note that the scatter in measured values of δ_{EDX} between growth batches and for different samples within a growth batch is too high to characterize precisely the effect of changing the starting composition δ_{nom} . We attempted to look for correlations of δ_{EDX} with other measured physical properties: lattice parameters, magnetic properties, and resistance; however we could not distinguish any correlations in the data.

B. Neutron Powder Diffraction

Figure 3 shows the neutron powder diffraction (NPD) data measured on two compositions at room temperature, $x_{\text{EDX}} = 0.10$ and 0.60 ; $x_{\text{EDX}} = 0.60$ represents the high-substitution limit. For $x_{\text{EDX}} = 0.60$ we measured data with $\lambda = 1.5403 \text{ \AA}$, while for $x_{\text{EDX}} = 0.10$ we additionally collected data with $\lambda = 1.1975 \text{ \AA}$ in order to optimize the data for site occupancy refinement; the data using neutrons with wavelength $\lambda = 1.1975 \text{ \AA}$ are shown for $x_{\text{EDX}} = 0.10$ in Fig. 3 to highlight the angular range measured, although the fitted parameters were obtained by co-refinement of the datasets from both wavelengths. The scale factor, background function, profile parameters, atomic coordinates, thermal factors, and site occupancies were refined. Exemplary fits to the data are shown with the solid black lines. Anisotropic broadening profile terms were required to fit all the peak widths simultaneously; adding an additional phase of the same structure to the single phase with anisotropic broadening hardly improves the fits, demonstrating a lack of phase separation and solubility of copper in each of these compounds. For the refinement starting models, we constrained the total amounts of metal to the values measured by EDX, while the range of values used for thermal factors and atomic coordinates spanned those in previous NPD and x-ray reports^{2,8,13,34,35}. Refining the copper content had little effect on χ^2 and did not correlate with other parameters, thus we kept it fixed to x_{EDX} . Refinements of the (2a) occupancy with various starting models consistently resulted in a fully occupied (2a) site. The two remaining site occupancy parameters may be

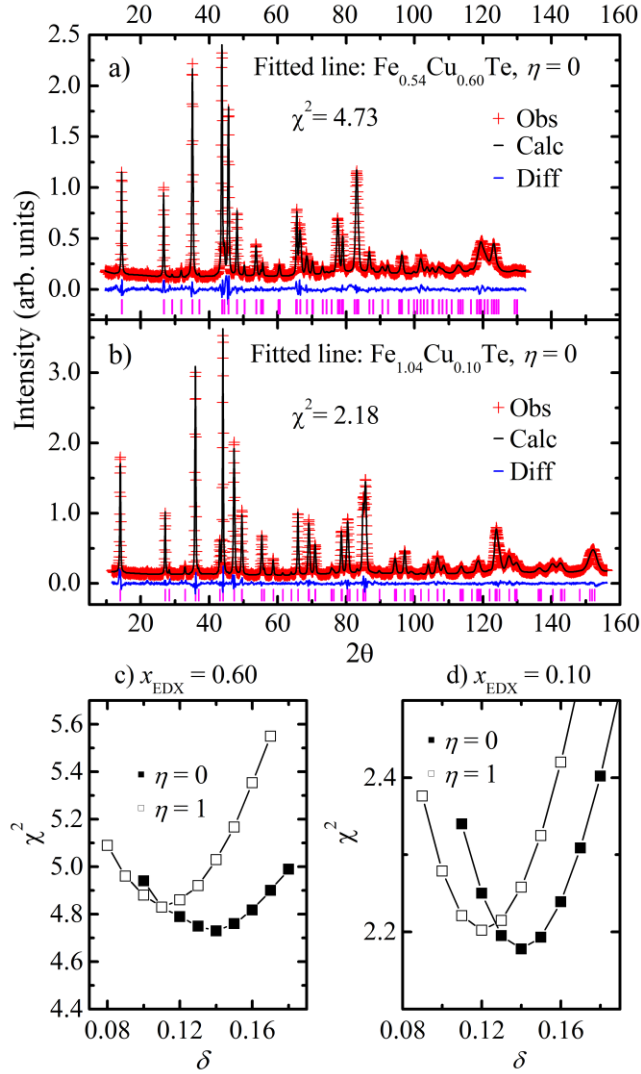


FIG. 3 Neutron powder diffractogram of a) $x_{\text{EDX}} = 0.60$ and b) $x_{\text{EDX}} = 0.10$ compounds. The goodness-of-fit χ^2 versus δ and η for c) $x_{\text{EDX}} = 0.60$ and d) $x_{\text{EDX}} = 0.10$ compounds.

represented by the variables (δ, η) . As in the EDX measurement, δ denotes the excess metal content that is equal to the total occupancy of the (2c) metal site divided by the tellurium occupancy. This gives the (2c) occupancy in these refinements. Given the interdependence of occupancy parameters in the refinement, it was necessary to fix the tellurium occupancy to 1. The inversion parameter η , describes the distribution of iron and copper over the two sites by the formula:

$$\eta = \begin{cases} 1 - \frac{O(\text{Cu}, 2c)}{x_{\text{EDX}}} & \text{when } x_{\text{EDX}} \leq \delta \\ 1 - \frac{O(\text{Cu}, 2c)}{\delta} & \text{when } x_{\text{EDX}} > \delta \end{cases} \quad (1)$$

with $O(\text{Cu}, 2c)$ being the copper occupancy on the (2c) metal site. Thus for $\eta = 0$, iron has maximum preference to be placed into the (2a) site; since our refinements suggest the (2a) site is fully occupied, we simply put as many iron atoms on (2a) as possible. For $\eta = 1$ copper is placed on the (2a) site only, with the remainder of the (2a) site and the (2c) site filled by iron. Increasing η shifts the best fits of δ to lower values and produces only marginal changes in χ^2 ; thus we cannot determine η but instead examine its effects on the range of best-fit values of δ . We constrained the height variables of interstitial metals: $Z_{\text{Fe}, 2c} = Z_{\text{Cu}, 2c} = Z_{\text{int}}$, and used one thermal factor for tellurium and another for the metals; using more thermal factors only marginally improved the fits. Since we have fixed the copper and tellurium contents, changing $\delta = (\text{Fe} + \text{Cu})/\text{Te}$ modifies the total iron content in the refinement model.

Figures 3c and 3d show the results of refinements performed while fixing values of the site occupancy parameters (δ, η) , while allowing all other parameters to vary freely. Fixing these parameters during refinement allows us to investigate cleanly the effects of each parameter on the fit. The solutions consistently lie on parabolae in the goodness-of-fit parameter χ^2 vs. δ (Figs. 3c-d); when the site occupancies are refined starting with the values at the minima of the parabolae, the refinements are found to be stable. As shown in Fig. 3c, the optimal occupancy of the (2c) site in the $x_{\text{EDX}} = 0.10$ sample is 0.12 Fe ($\eta = 1$), or 0.10 Cu and 0.04 Fe ($\eta = 0$). For the $x_{\text{EDX}} = 0.60$ sample, the optimal (2c) occupancies are 0.11 Fe, or 0.14 Cu. Comparison of the range of fitting values for these two samples suggests that the (2c) site occupancy does not change significantly between $0.10 \leq x_{\text{EDX}} \leq 0.60$. Since all possible values of η produce solutions between the ranges of δ obtained at the endpoints $\eta = 0$ and $\eta = 1$, these results suggest that the correlation between δ_{EDX} and x_{EDX} described in the previous section does not likely arise from an increase in the total metal content in the phase. The refined parameters for each sample are summarized in Table I, where the errors cover the range of values obtained for the best fit solutions with $\eta = 0$ and 1. We consider that better counting statistics which could be obtained by single crystal neutron diffraction might allow for an accurate refinement of η in future studies.

Very weak reflections with intensity at roughly 1% of that of the maximum reflection of the main phase were observed in each diffractogram; at this intensity they are almost indistinguishable from the background. 13 such features were observed for the $x_{\text{EDX}} = 0.60$ sample while only 8 were observed for the $x_{\text{EDX}} = 0.10$ data at $|Q| < 5.72 \text{ \AA}^{-1}$, none of which could be conclusively indexed to known phases in the open crystallography database³⁶. Therefore, the large values we observe for δ_{EDX} may be partly attributable to the formation of very slight amounts of impurity phases. Due to the limitations of our experiments,

TABLE I. Refined parameters from the neutron powder diffraction data (at room temperature). The atomic positions are provided in origin choice 2. Standard deviations are shown for the lattice parameters, which were consistent between fits, while the average and difference of refined values for the two site occupancy models are shown as the values before and within the parentheses for the other structural parameters.

Sample	$x_{\text{EDX}} = 0.10$	$x_{\text{EDX}} = 0.60$
c (Å)	6.2825(1)	6.1090(3)
a (Å)	3.8377(1)	3.9683(1)
δ_{NPD}	0.13(1)	0.13(2)
$U_{\text{iso}}(\text{Te})$ (Å ²)	0.0161(3)	0.0218(1)
$U_{\text{iso}}(\text{Fe/Cu})$ (Å ²)	0.0146(1)	0.0169(3)
Z_{Te}	0.2808(1)	0.2770(1)
Z_{int}	0.7074(1)	0.6984(6)
χ^2	2.19(1)	4.77(4)
wR_p	0.0579(2)	0.0644(3)
R_p	0.0464(2)	0.0502(3)

we cannot determine whether tellurium vacancies contribute to the large values of δ_{EDX} at high values of x_{EDX} at present.

C. Lattice Parameters

Figure 4 shows the room temperature lattice parameters of FCT as a function of copper concentration. We selected small pieces of crystal to grind for XRD, confirming their homogeneity by EDX measurements on both faces of the crystals. After grinding these crystals for the x-ray powder diffraction measurements, a small amount of NIST SRM 660b (LaB₆ powder) was mixed with the sample as a positional calibrant. The error in refined lattice parameters for each compound is smaller than 0.01 Å. Hence, the uncertainty in the refined lattice parameter is much smaller than the uncertainty in the concentration in the average copper content of the sample with respect to the EDX measurement, which was performed prior to grinding and therefore might only reflect the surface regions of the samples. We observe close agreement between the lattice parameters obtained by refinement of x-ray powder diffraction compared with those for the two samples refined by neutron powder diffraction.

While the c lattice parameter does not vary much for $x_{\text{EDX}} \leq 0.1$, the a lattice parameter shows a slight increase. For $x_{\text{EDX}} \geq 0.1$, the c lattice parameter contracts, and the a lattice parameter expands gradually with substitution, in agreement with the trends observed previously^{11,12}. However, the rate of change of lattice parameters with substitution in the region $x_{\text{EDX}} \geq 0.1$ is lower than that in the previous phase diagram¹¹. The lattice parameters obtained in the previous phase

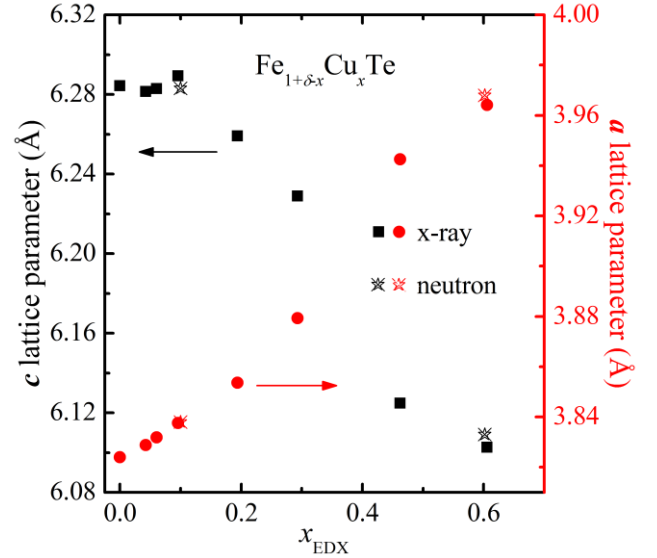


FIG. 4 Lattice parameters a and c as a function of Cu concentration x_{EDX} . See the text for details.

diagram at $x = 0.3$ ¹¹ are nearly equal to those we observe at $x_{\text{EDX}} = 0.46$. The lattice parameters we obtain in the region $0.46 \leq x_{\text{EDX}} \leq 0.60$ are close to values previously published for compounds with $x = 0.5, 0.55$ and 0.57 ^{13,16,19}. One possibility for the discrepancies between our lattice parameters and those of the previous phase diagram that is easily ruled out is that the values of x_{EDX} in the present study overcount the copper content due to the presence of impurity phases. Impurity phases of Cu, Cu₂O, CuO, or Cu_{1.4}Te would be expected to produce peaks of nearly-equal intensity (within a factor of 2) in the neutron powder diffractograms as those of the peaks from the main phase, if the mass fraction of each is the same. Therefore, given the lack of high intensity impurity peaks in the NPD measurements, we suggest that any impurity phase containing copper must contain a total mass of less than 1-2% of that of the main phase. Even if copper was distributed among several impurity phases, this could not account for the differences observed between the present phase diagram and the previous one¹¹. Therefore, if both measurements are correct, the differences must correspond to details of the main phase such as site occupancies: vacancies, excess metal δ , or η , which implies that one or more of these parameters may be sensitive to the growth conditions.

D. Susceptibility

Figure 5a shows the susceptibility of FCT as a function of copper concentration with the magnetic field applied parallel to the ab -plane. Sudden changes in the susceptibility χ occur for all samples at $T \leq 66$ K indicating the occurrence of magnetic transitions. None of our samples exhibit paramagnetism down to 10 K in contrast to the previous

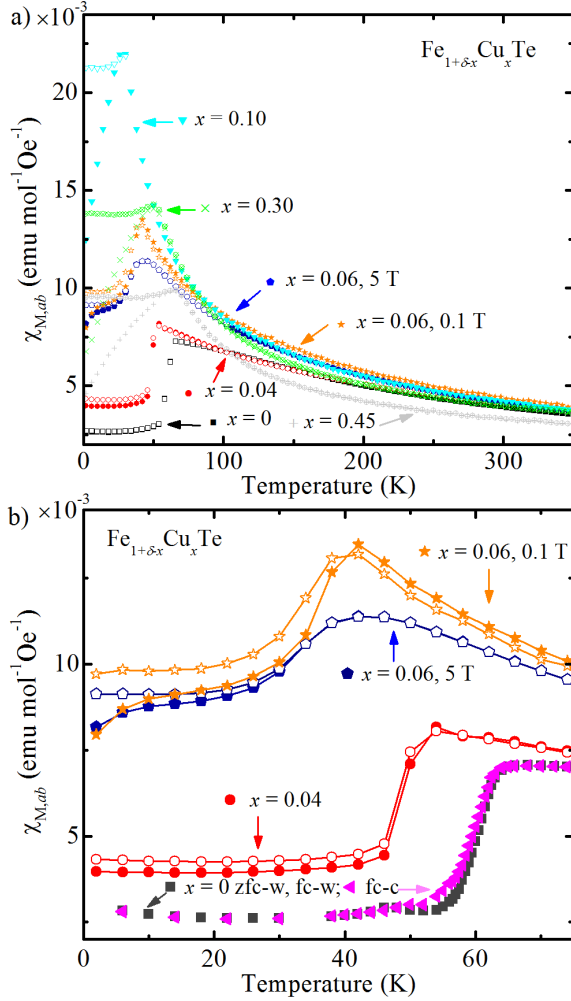


FIG. 5 a) Molar susceptibilities of a series of $\text{Fe}_{1+\delta-x}\text{Cu}_x\text{Te}$ compounds measured in zero-field-cooled (ZFC) and field-cooled (FC) measurements with applied fields of $\mu_0 H = 5\text{ T}$ for $x_{\text{EDX}} \leq 0.06$ and 0.1 T for $x_{\text{EDX}} \geq 0.06$. ZFC and FC are measured on warming. The field was applied in plane ($\mu_0 H \parallel ab$). The closed symbols are ZFC while the open symbols are FC. b) The same data, plotted in a limited temperature range $T \leq 75\text{ K}$ for $0 \leq x_{\text{EDX}} \leq 0.06$; and also showing field-cooled cooling (fc-c). Please note $1\text{ emu} / (\text{mol Oe}) = 4\pi \times 10^{-6}\text{ m}^3/\text{mol}$.

study with nominal concentration $x = 0.5$ and $\delta = 0^{16}$, nor did we observe signatures of a transition at $T = 256\text{--}308\text{ K}$ which was reported to occur in powdered crystals of nominal concentration $x = 0.5$ and $\delta = 0$ by Mössbauer and susceptibility measurements in well annealed samples^{14,15}. Our samples had higher nominal iron compositions and different preparation procedures than these samples; this implies that the details of the sample growth and heat treatment may be important to the properties. For samples with $x_{\text{EDX}} \geq 0.10$ the zero field cooled (ZFC) susceptibility decreases with decreasing temperature below the maximum in the susceptibility (which we label as the spin-glass

transition temperature, T_G) while in field-cooled (FC) measurements, the susceptibility is constant and approximately equal to the maximum value below T_G . These two characteristics are consistent with behavior expected for a spin-glass transition³⁷ and also consistent with the previous reports at 10% copper substitution¹¹. However, another report claimed that this compound exhibits a transition to a short-range antiferromagnetic state while they observed the same feature in susceptibility measurements¹². The divergence of $d\chi/dT$ at the transition temperature increases with increasing copper substitution up to $x_{\text{EDX}} = 0.10$, which might be understood in the antiferromagnetic state as the random field effect of copper³⁸ which will be discussed in detail later.

The data shown in Fig. 5 were measured at $\mu_0 H = 5\text{ T}$ for $x_{\text{EDX}} \leq 0.06$ and at $\mu_0 H = 0.1\text{ T}$ for $x_{\text{EDX}} \geq 0.06$ since the signal from what is presumably slight amounts of a ferrimagnetic Fe_3O_4 impurity phase obscures the signal from the main phase in $\mu_0 H = 0.1\text{ T}$ for $x_{\text{EDX}} \leq 0.04$; and in addition, no signal from Fe_3O_4 is observed for $x_{\text{EDX}} \geq 0.06$, but higher measuring fields can change the shape of the susceptibility transitions in these samples (not shown) which complicates the analysis. In order to compare the susceptibility at low copper substitution to that at high copper substitution, χ was measured for the $x_{\text{EDX}} = 0.06$ samples in $\mu_0 H = 0.1\text{ T}$ and 5 T . Although indicating a slight degree of magnetic saturation, the susceptibility data measured are nearly in agreement for the two different applied fields (Fig. 5b). A significant difference is that a sharp cusp (the temperature at which the maximum in the susceptibility occurs) appears at $T_{\text{cusp}} = 42\text{ K}$ in $\mu_0 H = 0.1\text{ T}$ and it is replaced by a broad maximum in $\mu_0 H = 5\text{ T}$.

As shown in Fig. 5b, the zero-field-cooled and field cooled susceptibilities measured on warming in field, χ_{ZFC} and χ_{FC} , show a thermal hysteresis in $x_{\text{EDX}} = 0$ with respect to the FC cooling curve ($T_N^{\chi} = 63.1\text{ K}$ in cooling and 63.5 K in warming determined from the intersection of linear fits to the susceptibility data above and below the maximum value) which is a signature of a first-order transition. Both ZFC and FC show a single feature with maximum susceptibility at $T_N^{\chi} = 54\text{ K}$ for $x_{\text{EDX}} = 0.04$ whereas $x_{\text{EDX}} = 0.06$ shows an additional feature below T_{cusp} which is most easily visible at temperatures below $T = 10\text{ K}$. Below this feature, ZFC and FC curves separate further with cooling. Such a two-featured $\chi(T)$ characteristic was consistently observed in at least four samples measured for each growth batch with $x_{\text{EDX}} = 0.06$. Unlike χ_{FC} in higher copper substituted compounds which remain constant below T_G , χ_{FC} in $x_{\text{EDX}} = 0.06$ is reduced below T_{cusp} , which indicates that this transition may be distinct from the spin-glass transitions. A similar feature was observed in $\text{Fe}_{1.13}\text{Te}$ which was explained as originating from non-bulk superconductivity³⁹. It is possible that our sample also exhibits non-bulk superconductivity although we did not observe any feature in the resistance data at this temperature. The lower temperature transition in $x_{\text{EDX}} = 0.06$

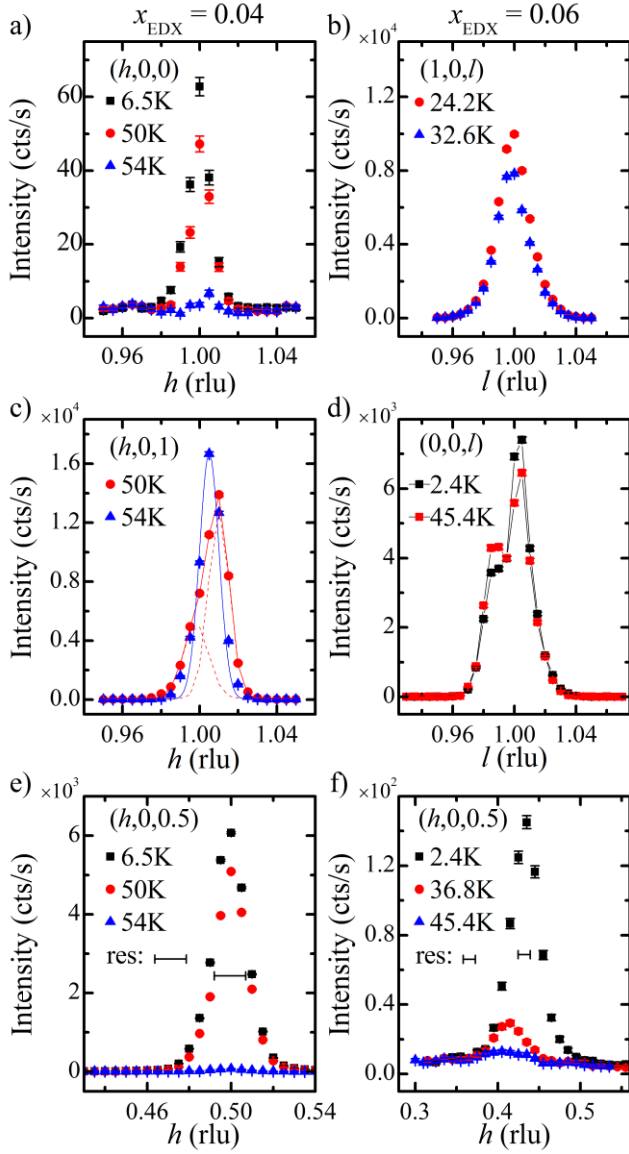


FIG. 6 Overview Q scans through structural and magnetic Bragg positions plotted with statistical error. For $x_{\text{EDX}} = 0.04$, structural a) $(1, 0, 0)$ and c) $(1, 0, 1)$ and e) magnetic $(0.5, 0, 0.5)$ peaks were measured at several temperatures. For $x_{\text{EDX}} = 0.06$, structural b) $(1, 0, 1)$ and d) $(0, 0, 1)$ and f) magnetic $(0.5-\epsilon, 0, 0.5)$ peaks were measured at several temperatures. Scans only at selected temperatures are shown here. The two line shapes drawn with dashed lines in panel c) denote two peak fitting. The instrumental resolution is denoted with bars in e) and f).

is quite subtle, and its transition temperature is difficult to determine with these data. We will discuss a clear transition observed in neutron scattering measurements in the next section.

Comparing χ_{ZFC} to χ_{FC} data, the susceptibility below and above the magnetic transition are lying on top of each other for both measurements in $x_{\text{EDX}} = 0$ (Fig. 5b). However, such

measurements showed that $\chi_{\text{FC}} - \chi_{\text{ZFC}} > 0$ at all temperatures below the maximum in χ for $x_{\text{EDX}} = 0.04$ and 0.06 (Fig. 5b). $\chi_{\text{FC}} - \chi_{\text{ZFC}} > 0$ is reproduced upon a subsequent ZFC procedure. Such behavior might occur if the antiferromagnetic domains form with moments preferably perpendicular to the field when field cooled, resulting in different magnitudes of χ_a and χ_b as expected from the magnetic symmetry of $\text{Fe}_{1+\delta}\text{Te}^2$ or if the sample moves due to the applied field during measurements. We found it notable that $\chi_{\text{FC}} - \chi_{\text{ZFC}}$ is nonzero for $\mu_0 H = 0.1 \text{ T}$ in $x_{\text{EDX}} = 0.06$ while $\chi_{\text{FC}} - \chi_{\text{ZFC}} = 0$ for $\mu_0 H = 5 \text{ T}$ in $x_{\text{EDX}} = 0$. We observed some sample-to-sample variation in the magnitude of χ which was less than 25% from the reported values and this might be due to sample shape effects.

Close inspection shows that the ZFC and FC procedures result in slightly different susceptibilities at temperatures above T_{cusp} in $x_{\text{EDX}} = 0.06$ in a field of 0.1 T . However, this difference is temperature-independent to $T = 350 \text{ K}$ (not shown), and is not observed in $\mu_0 H = 5 \text{ T}$ (Fig. 5b). We believe that it is likely due to the existence of slight amounts of an impurity phase, with a negligible contribution to the susceptibility in the higher field that saturates the impurity susceptibility. We also note the observation of signals at $T = 340 \text{ K}$ in some samples with $x_{\text{EDX}} \geq 0.15$ (not shown) which we also believe to be due to slight amounts of an unidentified impurity phase.

E. Single Crystal Neutron Scattering

In order to determine the properties of the low-temperature phases in the $x_{\text{EDX}} = 0.04$ and $x_{\text{EDX}} = 0.06$ samples, we monitored signals at several structural and magnetic Bragg peak positions at different temperatures using the single crystal neutron diffraction technique and summarize our results in Figs. 6 – 10.

In Figure 6, we show overview scans for structural $(h, 0, l)$ ($h = l = \text{integer}$) peaks and magnetic $(h, 0, 0.5)$ peaks at selected temperatures. For the $x_{\text{EDX}} = 0.04$ sample we monitored structural Bragg peaks at $Q = (1, 0, 0)$ and $(1, 0, 1)$ (Figs. 6a and 6c). The observed signals at the $(1, 0, 0)$ Bragg peak position indicate that the low temperature phase in $x_{\text{EDX}} = 0.04$ is in monoclinic symmetry since the $(1, 0, 0)$ is disallowed within the known tetragonal and orthorhombic symmetries of $\text{Fe}_{1+\delta}\text{Te}$ but allowed in the monoclinic symmetry previously reported for $\text{Fe}_{1+\delta}\text{Te}^6$. For further investigation of the low temperature structure in $x_{\text{EDX}} = 0.04$, we measured the structural $(1, 0, 1)$ peak and observed that at $T = 50 \text{ K}$ (below the transition) the peak can be fitted with two Gaussian line shapes in the $[h, 0, 0]$ scan (Fig. 6c) indicating two different in-plane lattice parameters.

For the $x_{\text{EDX}} = 0.06$ sample, we did not observe any signal at $(1, 0, 0)$ at the lowest temperature in our measurement ($T = 2.5 \text{ K}$) and observed a single peak at the $(1, 0, 1)$ Bragg peak position (Fig. 6b). Neither peak splitting nor broadening of the peak was observed at $Q = (1, 0, 1)$. However, we observed an increase of intensity of $(1, 0, 1)$

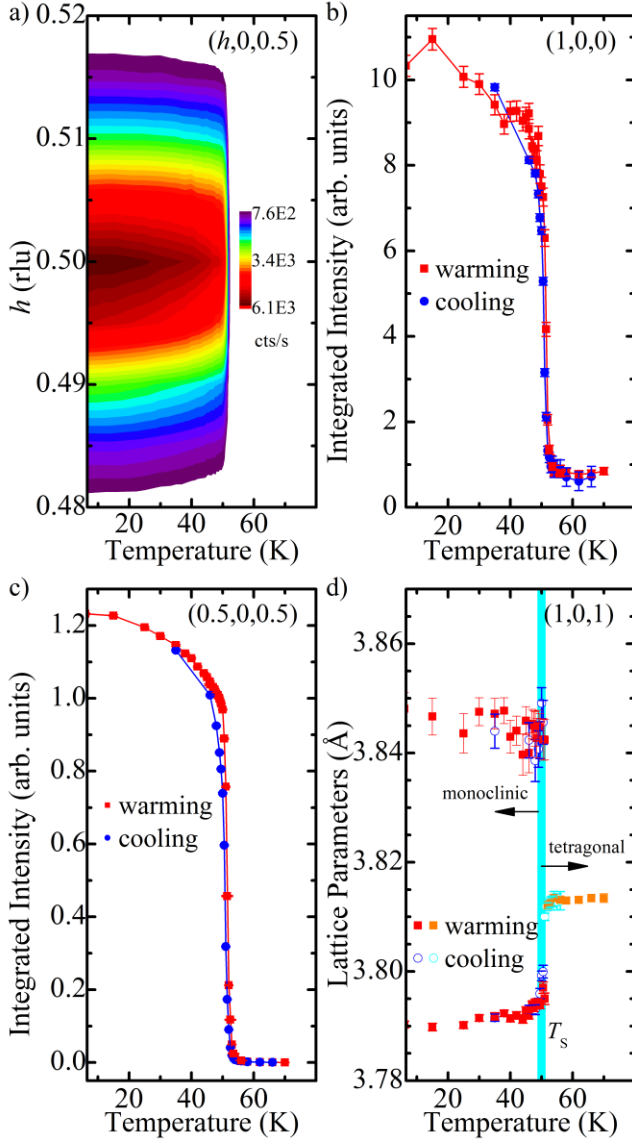


FIG. 7 The AFM and structural order parameters for the $x_{\text{EDX}} = 0.04$ compound plotted with statistical error. a) Contour map of magnetic scattering around $(0.5, 0, 0.5)$ Bragg peak, measured on warming. b) Integrated intensity of $(1, 0, 0)$ Bragg peak as a structural order parameter. Note that a small background which is temperature-independent exists between 54 and 70 K above T_N . c) The AFM order parameter obtained from the integrated intensity at $(0.5, 0, 0.5)$ d) Temperature dependent lattice parameters extracted from fits to $[h, 0, 1]$ scans show the tetragonal-to-monoclinic transition.

Bragg peak as the temperature was lowered. This increase in intensity is likely due to extinction release^{40,41} caused by a symmetry lowering structural transition. As any changes in the $(0, 0, 1)$ Bragg peak are negligible in temperature (Fig. 6d) the transition likely involves in-plane structural

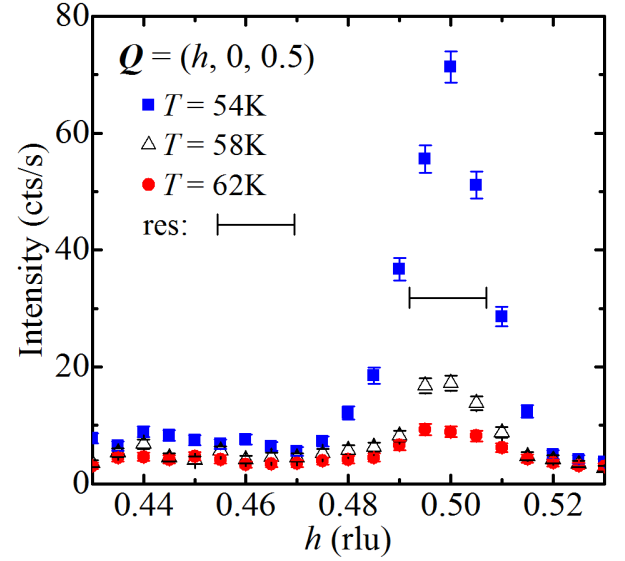


FIG. 8 Weak magnetic scattering in $x_{\text{EDX}} = 0.04$ (above T_N) plotted with statistical error

parameters only. We note that the determination of the exact low temperature structure for $x_{\text{EDX}} = 0.06$ is beyond the scope of our current paper. It should be noted that the $(0, 0, 1)$ scan contains two peaks (Fig. 6d) indicating a possible phase separation with two different c-axis lattice parameters, which was not detected in x-ray powder diffraction measurements.

We also measured signals at $Q_{\text{AFM}} = (h, 0, 0.5)$ and show $[h, 0, 0]$ scans of $x_{\text{EDX}} = 0.04$ and 0.06 samples in Figs. 6e and 6f, respectively. We observed a sharp resolution-limited peak at $Q_{\text{AFM}} = (0.5, 0, 0.5)$ in $x_{\text{EDX}} = 0.04$, which is commensurate and consistent with the bicollinear AFM structure². In $x_{\text{EDX}} = 0.06$, the magnetic peak is markedly broader than the instrumental resolution, and appears at an incommensurate position ($h = 0.433 \pm 0.002$ at $T = 2.5$ K); only weak intensity which could not be properly fitted to a peak is observed at $T = 45$ K as shown in Fig. 6f.

For further investigations on the structural and magnetic phase transitions in these materials, we measured the above-mentioned structural and magnetic Bragg peaks as a function of temperature and show the structural and magnetic order parameters in Fig. 7 for $x_{\text{EDX}} = 0.04$ and Fig. 9 for $x_{\text{EDX}} = 0.06$. Figure 7a shows a temperature dependent contour map of the intensity around the $(0.5, 0, 0.5)$ magnetic peak in $x_{\text{EDX}} = 0.04$. Figure 7c shows a magnetic order parameter obtained by integrating the intensities of the $(0.5, 0, 0.5)$ magnetic Bragg peak. Measurements during cooling and warming exhibit thermal hysteresis; $T_N = 50.75$ K during cooling and 51.5 K upon warming. The observed transition temperature by neutron measurements is consistent with T_N^x . We conclude from our neutron measurements that the AFM transition is first order in $x_{\text{EDX}} = 0.04$. A close inspection reveals a weak, but resolution limited scattering that remains at the commensurate position above T_N (up to 62 K), with intensity 2-3 orders of magnitude lower than that at

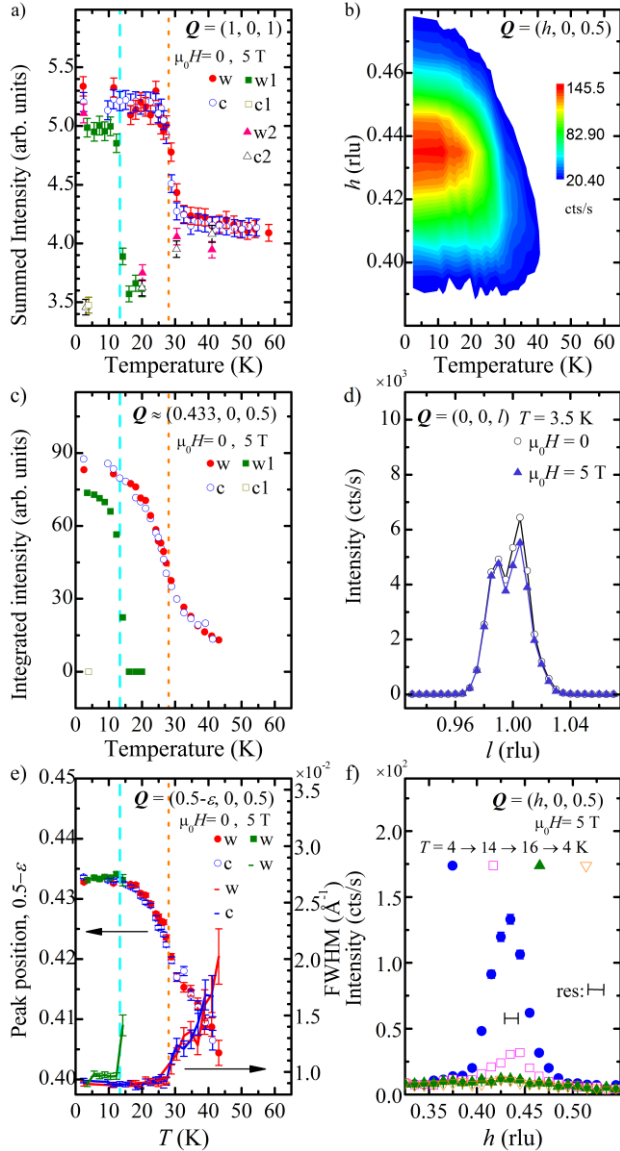


FIG. 9 Order parameters for the $x_{\text{EDX}} = 0.06$ sample, and sample alignment in field plotted with statistical error. The lower and upper dashed lines in panels a) c) and e) denote T_M and T_{SRO2} , respectively a) Structural order parameter (summation) b) Contour map of magnetic scattering measured on warming c) Magnetic order parameter (integration) d) (0, 0, 1) scan before and after applying field e) Incommensurability (symbols) and FWHM (lines) of AFM order; f) Magnetic peak measured in field while warming and cooling across T_M

temperatures just below T_N (Fig. 8). The existence of weak scattering is in agreement with previous studies of $\text{Fe}_{1+\delta}\text{Te}$, and lightly copper-substituted $\text{Fe}_{1+\delta}\text{Te}$, although such scattering has been reported as incommensurate and short-range^{2,12}, in contrast to the magnetism in the present sample which is commensurate and resolution limited at all temperatures measured (Fig 8).

The structural order parameters at $\mathbf{Q} = (1, 0, 0)$ and $(1, 0, 1)$ for $x_{\text{EDX}} = 0.04$ were also investigated. Since the $(1, 0, 0)$ peak is disallowed in the high temperature tetragonal structure, the occurrence of signals at $\mathbf{Q} = (1, 0, 0)$ is a good structural order parameter while the lattice parameter splitting obtained from two-peak fit in the $(1, 0, 1)$ peak also well presents a structural order parameter (Figs. 7b and 7d, respectively). We observe that the structural transition occurs at the same temperature as T_N during cooling and warming, which exhibits the same thermal hysteresis ($T_S = 50.75 \text{ K}$ and 51.5 K). Hence, we conclude that the AFM transition and the structural transition occurs simultaneously and as first order transitions in $x_{\text{EDX}} = 0.04$.

We now turn to the structural and magnetic transitions in the $x_{\text{EDX}} = 0.06$ compound. We first discuss our observation in an ambient condition, that is $\mu_0 H = 0 \text{ T}$. We summed all counts in the \mathbf{Q} range measured through the structural $(1, 0, 1)$ peak and found that the intensity increases sharply at $T = 28 \text{ K}$, which remains constant above this temperature. As discussed earlier, we believe that this temperature is associated with an in-plane structural distortion and we define $T = 28 \text{ K}$ to be the structural transition temperature T_S . As there is no evidence for thermal hysteresis our results are consistent with a second order transition through $T_S = 28 \text{ K}$.

Figure 9b shows a contour plot of magnetic scattering in $x_{\text{EDX}} = 0.06$ measured at $\mathbf{Q}_{\text{AFM}} = (h, 0, 0.5)$ without an applied field ($\mu_0 H = 0 \text{ T}$). We fit the $(h, 0, 0.5)$ magnetic peak with the Lorentzian peak shape function and present the integrated intensities (Fig. 9c), the full-width-at-half-maximum (FWHM, Fig. 9e) and the peak position (Fig. 9e) as a function of temperature. We note that the instrumental resolution is convoluted in the analysis of the correlation length which is shown in Fig. 10. Weak signals at \mathbf{Q}_{AFM} appear below $T = 43.2 \text{ K}$ and increase gradually until the slope maximizes at $T = 28 \text{ K}$. The analysis of the FWHM and the correlation length of the magnetic peak demonstrates that the magnetic ordering is short ranged when it appears at the short range magnetic transition temperature $T_{\text{SRO1}} = 43.2 \text{ K}$ and the magnetic correlation length is temperature dependent down to $T = 28 \text{ K}$ (Fig. 9e and Fig. 10). With further cooling, the FWHM reaches its minimum value (not resolution-limited) with a correlation length of 250 \AA and remains constant below T_S as shown in Fig. 9e and Fig. 10. We define the second short range order transition to be the temperature where the FWHM becomes constant and the magnetic intensity increases most rapidly: $T_{\text{SRO2}} = 28 \text{ K}$. Although a short-range magnetic order was reported to coexist and compete with another long-range magnetic order in $\text{Fe}_{1.12}\text{Te}$ compound², we did not observe additional magnetic peaks in the measured \mathbf{Q} range ($0.315 \leq h \leq 0.54$) but the short-range order alone. The observed short-range order may be caused by short-range bond-length modulations which were claimed in $\text{Fe}_{1.09}\text{Te}$ compounds⁶. However, details of the nature of the short range order in this compound call for further study.

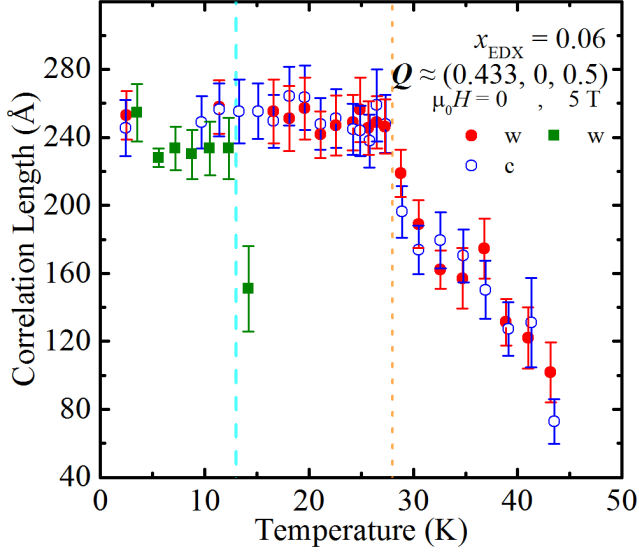


FIG. 10 The spin correlation length along the $[h, 0, 0]$ direction for $x_{\text{EDX}}=0.06$ compound, corrected for the instrumental resolution of SPINS with statistical error. The field conditions are indicated in the figure; the lower and upper dashed lines indicate T_M and T_{SRO2} , respectively

In addition to the observation of the short-range magnetic order, we also observe that the magnetic peak is incommensurate at all temperatures measured and the peak position changes smoothly from $h \approx 0.40$ toward $h = 0.433$ (the value at $T = 2.4$ K) as shown in Fig. 9e, which corresponds to a real space periodicity of approximately seven magnetic unit cells in every sixteen structural cells along the a axis. The position is constant below $T \approx 13$ K (Fig. 9e). It is interesting to note that $T_{\text{cusp}} = 42$ K in the susceptibility measurements coincides with T_{SRO1} but no additional feature was observed in the susceptibility near $T_{\text{SRO2}} = T_S$.

Altogether, the short-range magnetic order occurs at $T_{\text{SRO1}} = 43.2$ K above the in-plane structural transition at $T_S = 28$ K which coincides with T_{SRO2} . Since we observe continuous evolution of order parameters, continuous changes in FWHM, and no thermal hysteresis, we conclude that each of these transitions is second order in nature. Interestingly, we did not observe a structural transition at T_{SRO1} . However, based on the symmetry requirements for the AFM order at Q_{AFM} , a symmetry lowering transition should accompany T_{SRO1} but it may be too small to be detected with the given instrumental resolution.

Under an applied field ($\mu_0 H = 5$ T) parallel to the $[0, 1, 0]$ direction in our scattering geometry, we observed surprising results in both the structural and magnetic transitions. In order to ensure the sample alignment under applied magnetic fields, we first measured the structural Bragg peaks without a field ($\mu_0 H = 0$ T) and then again after applying a field ($\mu_0 H = 5$ T). We observed a reduction ($\sim 10\%$) in the intensity of all peaks but the positions did not change which indicates a good sample alignment under an applied field (Fig. 9d).

While the cause of the decrease in the peak intensities with $\mu_0 H = 5$ T is unknown it might be due to a subtle rotation of the sample. Knowing that our sample alignment is good under $\mu_0 H = 5$ T, we measured the temperature dependent structural $(1, 0, 1)$ peak under $\mu_0 H = 5$ T. As shown with w1 and c1 in Fig. 9a, the Bragg peak intensity did not change much until it suddenly dropped between 12 and 14 K during warming. The magnetic $(h, 0, 0.5)$ peak was monitored simultaneously and showed the same behavior (disappeared completely at 16 K) as shown with w1 and c1 in Fig. 9c and 9f. To complete the temperature dependence, we then measured $(1, 0, 1)$ and $(h, 0, 0.5)$ peaks while cooling in the field and found that the signals do not increase across $T \approx 14$ K. We considered that this observation might be due to a misalignment of our sample during a temperature cycle under fields so we warmed the temperature well above T_{SRO2} to check the sample alignment then recovered the intensity at $(1, 0, 1)$ (Fig. 9a). We cooled our sample to $T = 4$ K again without an applied magnetic field and recovered the intensity of $(1, 0, 1)$ again which confirms the alignment during temperature cycles. We also recovered the intensity at Q_{AFM} and the original temperature dependence which confirms the absence of a remanent field. At $T = 4$ K, we applied a magnetic field ($\mu_0 H = 5$ T) and measured the temperature dependence of the structural $(1, 0, 1)$ peak at selected temperatures as denoted as w2 and c2 in Fig. 9a. We thus reproduced the results while warming in field, and confirmed that the field-cooled behavior is consistent whether the sample is cooled from $T = 80$ K or $T = 20$ K. Therefore this transition is metastable in field and both the structural and magnetic transitions occur abruptly at $T_M = 13$ K. In the magnetic state below T_M , the incommensurability does not change and the peak appears at a value of $h = 0.433$ which may indicate a first-order lock-in transition.

The absence of the magnetic intensity in the field cooled measurements in this compound may be seen as a strong random field effect of the Cu impurities, where the random fields are generated by the Fishman-Aharony mechanism³⁸. In site diluted antiferromagnets, field-cooling through the magnetic transition induces a “domain state” in which magnetic moments around the impurities are, on average, paramagnetic with the applied field; these paramagnetic moments may limit the long range ordering^{42–44}. It may be possible for a strong random field effect to completely inhibit the magnetic ordering as observed in our case. The increase in the divergence of $d\chi/dT$ at the transition for $x_{\text{EDX}} \leq 0.10$ is also suggestive of a random field scenario³⁸.

Furthermore, upon warming in the field between T_M and 30 K as well as in cooling in the field at all temperatures below 30 K, the intensity of the $(1, 0, 1)$ peak is much lower than the field-free values (Fig. 9a). This low intensity implies that another structure type may exist under these conditions, possibly different from the tetragonal structure above the transition and from the structure below the transition in zero field (which we have not identified). The simultaneous first-order magnetic and structural transitions at $T_M = 13$ K

TABLE II. Fitted exponent of $\log(R)$ vs. $\log(T)$ data in different temperature ranges

Temperature Range (K)	$m(x_{\text{EDX}}=0.52)$	$m(x_{\text{EDX}}=0.55)$
20-150K	0.825(1)	1.026(1)
150-300K	1.011(1)	1.235(1)

indicate a strong coupling between magnetism and structure. Hence if the structure without the AFM at $13 \text{ K} < T < 30 \text{ K}$ remains stable under field cooling below T_M , the AFM transition will not occur. Further study is necessary to determine the details of each of these transitions at T_M as well as another possible transition between T_M and 30 K ($\approx T_{\text{SRO2}}$).

F. Resistance

Figure 11 shows the normalized electrical resistance data $R(T)/R(300 \text{ K})$ of $\text{Fe}_{1+\delta-x}\text{Cu}_x\text{Te}$ measured as a function of temperature between $T = 2 \text{ K}$ and 300 K . As the copper concentration increases, the resistance anomaly moves to lower temperatures, and is absent in samples which only exhibit spin-glass transitions at low temperature i.e. $x_{\text{EDX}} \geq 0.1$ (Figs. 11a and 11b). The normalized resistance increases with both increasing copper concentration and temperatures, aside from the sample with $x_{\text{EDX}} = 0.04$ that has higher normalized resistance than the samples with $x_{\text{EDX}} = 0.06$ or $x_{\text{EDX}} = 0.1$ between $T = 53 \text{ K}$ and 300 K . Such behavior was reproduced for samples from two different growth batches for each composition. The higher normalized resistance in $x_{\text{EDX}} = 0.04$ suggests that the samples in the previous study¹¹ may have different site occupancy parameters (δ , η , and/or vacancies), and/or different nonequilibrium characteristics (phase segregation parameters, or defects) due to the different growth methods used.

Figure 11b shows the anomalies in resistance measured upon cooling and subsequent warming for $x_{\text{EDX}} \leq 0.06$. For $x_{\text{EDX}} = 0$ and 0.04 , we found a thermal hysteresis upon cooling and warming, which indicates first-order transitions. This is consistent with the observation in neutron measurements for $x_{\text{EDX}} = 0.04$; therefore, the observed transition in the resistance indicates the Neel transition. We define the transitions $T_N^{\text{resistance}}$ at the local maxima in the resistance values, $T_N^{\text{resistance}} = 65.5 \text{ K}$ (warming) and 64.5 K (cooling) for $x_{\text{EDX}} = 0$, and $T_N^{\text{resistance}} = 52 \text{ K}$ (warming) and 50.5 K (cooling) for $x_{\text{EDX}} = 0.04$. Unlike the sharp and hysteretic anomalies in $x_{\text{EDX}} = 0$ and 0.04 , the sample with $x_{\text{EDX}} = 0.06$ shows a broad maximum centered at $T_{\text{max}}^{\text{resistance}} = 34 \sim 36 \text{ K}$ and a broad minimum centered at $T_{\text{min}}^{\text{resistance}} = 22 \sim 25 \text{ K}$, where the range of values estimated for the extrema depends on whether a flat or sloping background is taken. Below $T_{\text{min}}^{\text{resistance}}$ the resistance increases with decreasing temperature which is different to the behavior at lower copper substitution, but similar to the effects of excess iron in $\text{Fe}_{1+\delta}\text{Te}$ ^{5,45} where it has been attributed to the closing

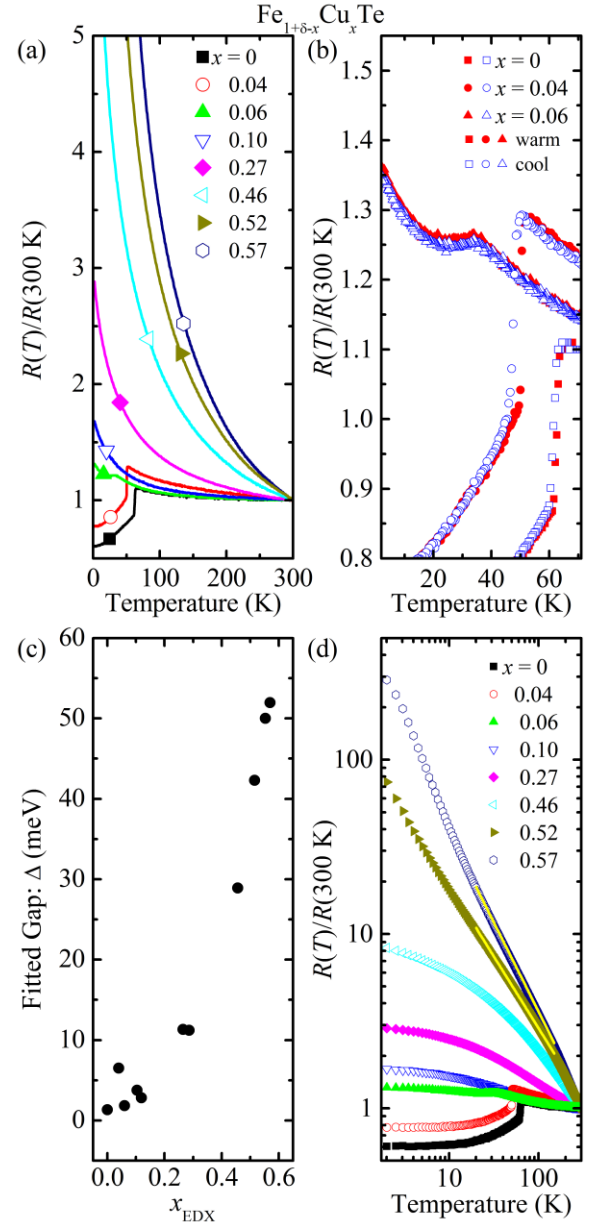


FIG. 11 Normalized resistance of $\text{Fe}_{1+\delta-x}\text{Cu}_x\text{Te}$ compounds. a) Data with linear axes and plotted in a limited range of normalized resistance, for comparison of samples. b) Measurements upon cooling and subsequent warming for $x_{\text{EDX}} \leq 0.06$. c) Fitted energy gap versus x_{EDX} for the data with $200 \text{ K} \leq T \leq 300 \text{ K}$. d) Data with logarithmic axes and plotted in the full range of normalized resistance. Yellow lines are power law fits as described in the text

of a spin gap in the helical AFM phase. Because our neutron measurement does not rule out the helical magnetic structure in our sample, the increase of the resistance at $T < T_{\text{min}}^{\text{resistance}}$ may be due to the closing of the spin gap. $T \approx 28 \text{ K}$ is between the temperatures of the local maximum and minimum in resistance so we associate this transition with $T_S = T_{\text{SRO2}} = 28 \text{ K}$ determined in neutron measurements, noting that no

resistance anomaly was observed at $T_{\text{SRO1}} = 43.2$ K which is far above the maxima and minima in the resistance of $x_{\text{EDX}} = 0.06$. Furthermore, we have observed the appearance of transitions at temperatures close to T_{M} (which are not shown) under the applied field⁴⁶.

In order to gain insight into the relevant transport processes of $\text{Fe}_{1+\delta-x}\text{Cu}_x\text{Te}$, we analyze the resistance data using models that have been proposed to govern the transport in $\text{Fe}_{1+\delta}\text{Te}$ ⁴⁷ or in Cu substituted compounds with $x \approx 0.5$ ¹⁶⁻¹⁸. As the samples become less conductive upon copper substitution, we tried fitting to an activated model, commonly used to model an intrinsic semiconductor or insulator⁴⁸ and written as

$$R(T) \propto \frac{1}{qn\mu} \propto T^{-m} e^{-\frac{\Delta}{2kT}} + R_0 \quad (2)$$

where the exponent m includes temperature dependences of the carrier concentration n and mobility μ , Δ is the band gap, and R_0 is a constant. We set $m = 0$ and performed fits for Δ by fitting $\ln(R)$ vs $1/T$ to a line between $T = 200$ K and 300 K, and extracted the Δ values shown in Fig 11c. If the model is valid, these fits suggest that Δ increases from 1 to ~ 50 meV in the range $0 \leq x_{\text{EDX}} \leq 0.57$, as shown in Fig 11c; the values at high substitution are intermediate to $\Delta = 23$ -70 meV as reported in previous studies for $x \approx 0.5$ ^{17,18}.

We also tried power-law scaling of the resistance that was observed in previous studies in samples with $x \approx 0.5$ with exponents of $m = 1.15$ ¹⁶ or $m = 1$ ¹⁸, which the authors¹⁶ attributed to the realization of the condition $\Delta \approx 0$ in Equation (2). The power-law scaling behavior was first observed in semimetals such as α -Sn or HgTe^{49,50}. We present R vs. T on a logarithmic scale in Fig. 11d. The resistance in $\log(R)$ vs. $\log(T)$ is nearly linear for samples with $x_{\text{EDX}} = 0.52$ and 0.57. The fits of the raw data between 20 K and 150 K for $x_{\text{EDX}} = 0.52$ and $x_{\text{EDX}} = 0.57$ using Equation (2) with a mesh of $\Delta = 0.1:500$ meV and $m = -3:0.01:3$ yield the best fits with $\Delta = 0$ (solid lines in Fig. 11d). In Table II, we present variation of the fitted exponents when different temperature ranges of data were fitted. Similar to a previous study on FCT with $x \approx 0.5$, the deviation from the power law fit was greatest at low temperatures¹⁸. Although the resistance of the $x_{\text{EDX}} = 0.04$ sample can be fitted to a power law above its transition with an exponent close to zero, the $x_{\text{EDX}} = 0$ sample does not fit well to a power law. Thus, we believe the power law behavior is less relevant for these low-substituted samples.

Another form which has been suggested to fit the resistance above the Neel transition temperature in iron-telluride is⁴⁷:

$$R(T) \propto \log(1/T) + R_0 \quad (3)$$

where R_0 is constant. This form is suggested to arise from a weak localization effect involving electronic scattering at

interstitial sites. Our fits to the data for the samples with $x_{\text{EDX}} = 0$ and 0.04 above their transition temperatures were good but failed to fit the data far above T_N for $x_{\text{EDX}} = 0$. This form could not fit any significant temperature range of the data for other compositions.

Finally, we attempted to fit the data to variable-range hopping models which describe temperature-activated conduction when electronic states are localized due to Coulomb repulsion or disorder⁵¹. The variable-range hopping formula is:

$$\ln(R(T)) \propto (1/T)^{1/(d+1)} + R_0 \quad (4)$$

where the exponent d is the dimensionality of the system. While this model with $d = 3$ has been suggested to provide a good fit to the resistance curves in copper-substituted $\text{FeSe}_{0.96}$ ²⁶, $\text{FeSe}_{1-y}\text{Te}_y$ ²⁷, and FCT with $x \approx 0.5$ ¹⁷, we found that it does not provide a good fit to any of our data over any appreciable temperature range and the fit is especially poor at low temperatures where the closest agreement with the model should occur⁵¹. The fits with varying d in temperature ranges between 2 and 30 K, between 2 and 120 K, and between 70 and 300 K are unstable as indicated by large uncertainty or nonphysical values of d . Another recent work also reported the lack of fit of the variable range hopping model to the resistance of samples with $x \approx 0.5$ ¹⁸.

Taken together, we find that the variable range hopping model cannot fit any of the data. The data for samples with $x_{\text{EDX}} = 0$ and 0.04 could be fit by the $R \sim -\ln(T)$ model, which is ascribed to localization due to electronic scattering at the interstitial sites⁴⁷. For samples with $x_{\text{EDX}} = 0.52$ and $x_{\text{EDX}} = 0.57$, the resistivity data can be well-fitted by power laws across a large region of temperature with the exponent $m \approx 1$ that may be interpreted as support for a model of localized and diffusive charge transport as claimed in previous reports^{16,18}. Whereas the activated model can describe the high temperature data for each sample, fitting the low temperature data can only be done with the weak localization model in the low-substitution limit or with the zero band gap model in the high substitution limit. Although it is difficult to determine conclusively, our observations suggest that local interactions are important factors in the transport mechanisms.

4. SUMMARY AND CONCLUSION

We have studied the stoichiometry, crystal structure, magnetism, and electrical resistance of $\text{Fe}_{1+\delta-x}\text{Cu}_x\text{Te}$ single crystals grown by the modified Bridgman method. Similar to other metal substituted iron-telluride systems, copper substitution causes suppression of the magnetic and structural transitions. From our studies of susceptibility, resistance, and neutron measurements, we constructed a phase diagram of $\text{Fe}_{1+\delta-x}\text{Cu}_x\text{Te}$ which we show in Fig. 12.

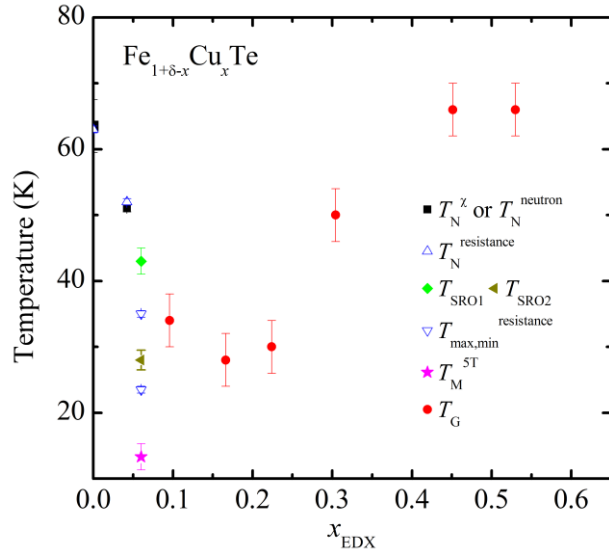


FIG. 12 Magnetic phase diagram of $\text{Fe}_{1+\delta-x}\text{Cu}_x\text{Te}$ compounds. See text for details of the notation.

The long-range AFM transition is rapidly suppressed with only slight copper substitution. When $x_{\text{EDX}} = 0.06$, the long-range AFM order is replaced by short-range ordering which exhibits two transitions (T_{SRO1} and T_{SRO2}). Under $\mu_0 H = 5\text{T}$, we observed a metastable magnetic transition at T_M . At $x_{\text{EDX}} \geq 0.1$, a spin glass phase appears at a minimum of $T_G = 28\text{ K}$ at $x_{\text{EDX}} = 0.16$ and T_G increases with further copper substitution.

We find that the structural and antiferromagnetic transitions occur at the same temperature and show first-order nature in $x_{\text{EDX}} = 0$ and 0.04 . The AFM ordering is commensurate in these compounds, and gives way to incommensurate short-range order in $x_{\text{EDX}} = 0.06$. The short-range order appears continuously without a detectable structural transition and at lower temperature another short-range ordering transition, defined by the saturation of the

correlation length (250 \AA), occurs simultaneously with a structural transition. A first-order metastable magnetic transition appears at $T_M \approx 13\text{ K}$ under an applied magnetic field which indicates strong coupling between structure and magnetism. The behavior of the magnetic component of this transition may indicate random field effects. Furthermore, detailed study of the resistance data indicates the localized nature of the transport at all compositions within the phase diagram. These results suggest that strong in-plane field effects present challenges to understanding the magnetism in the iron chalcogenides.

ACKNOWLEDGEMENTS

We are grateful to Dung Hai Lee, James Analytis, and Toni Helm for stimulating discussions, and to Daniel Lee, James Wu, and Tim Teague for experimental support. We acknowledge the support of the National Institute of Standards and Technology, U.S. Department of Commerce, in providing the neutron research facilities used in this work. Work at Lawrence Berkeley National Laboratory and UC Berkeley was supported by the Office of Basic Energy Sciences, Division of Materials Science and Engineering, US Department of Energy, under Contracts No. DE-AC02-05CH11231 and Office of Basic Energy Sciences, U.S. DOE under Grant No. DE-AC03-76SF008. Certain commercial equipment are identified in this paper to foster understanding. Such identification does not imply recommendation or endorsement by the National Institute of Standards and Technology, nor does it imply that the equipment identified are necessarily the best available for the purpose

¹ Y. Xia, D. Qian, L. Wray, D. Hsieh, G.F. Chen, J.L. Luo, N.L. Wang, and M.Z. Hasan, Phys. Rev. Lett. **103**, 037002 (2009).

² E.E. Rodriguez, C. Stock, P. Zajdel, K.L. Krycka, C.F. Majkrzak, P. Zavalij, and M.A. Green, Phys. Rev. B **84**, 064403 (2011).

³ Z. Xu, Ph.D. Thesis, City University of New York, 2011.

⁴ I.A. Zaliznyak, Z.J. Xu, J.S. Wen, J.M. Tranquada, G.D. Gu, V. Solovyov, V.N. Glazkov, A.I. Zheludev, V.O. Garlea, and M.B. Stone, Phys. Rev. B **85**, 085105 (2012).

⁵ E.E. Rodriguez, D.A. Sokolov, C. Stock, M.A. Green, O. Sobolev, J.A. Rodriguez-Rivera, H. Cao, and A. Daoud-Aladine, Phys. Rev. B **88**, 165110 (2013).

⁶ D. Fobes, I.A. Zaliznyak, Z. Xu, R. Zhong, G. Gu, J.M. Tranquada, L. Harriger, D. Singh, V.O. Garlea, M.

Lumsden, and B. Winn, Phys. Rev. Lett. **112**, 187202 (2014).

⁷ W. Bao, Y. Qiu, Q. Huang, M.A. Green, P. Zajdel, M.R. Fitzsimmons, M. Zhernenkov, S. Chang, M. Fang, B. Qian, E.K. Vehstedt, J. Yang, H.M. Pham, L. Spinu, and Z.Q. Mao, Phys. Rev. Lett. **102**, 247001 (2009).

⁸ R. Vienneis, Acta Phys. Pol. A **121**, 928 (2012).

⁹ R. Hu, E.S. Bozin, J.B. Warren, and C. Petrovic, Phys. Rev. B **80**, 214514 (2009).

¹⁰ J. Janaki, T. Geetha Kumary, N. Thirumurugan, A. Mani, A. Das, G. V. Narasimha Rao, and A. Bharathi, J. Supercond. Nov. Magn. **25**, 209 (2011).

¹¹ H. Wang, C. Dong, Z. Li, J. Yang, Q. Mao, and M. Fang, Phys. Lett. A **376**, 3645 (2012).

¹² J. Wen, Z. Xu, G. Xu, M. Lumsden, P.N. Valdivia, E. Bourret-Courchesne, G. Gu, D.-H. Lee, J.M. Tranquada, and R.J. Birgeneau, Phys. Rev. B **86**, 024401 (2012).

- ¹³ A.-M. Lamarche, J.C. Woolley, G. Lamarche, I.P. Swainson, and T.M. Holden, *J. Magn. Magn. Mater.* **186**, 121 (1998).
- ¹⁴ A. Rivas, F. Gonzalez-Jimenez, L. D'Onofrio, E. Jaimes, M. Quintero, and J. Gonzalez, *Hyperfine Interact.* **134**, 115 (2001).
- ¹⁵ A. Rivas, F. Gonzalez-Jimenez, L. D'Onofrio, E. Jaimes, M. Quintero, and J. Gonzalez, *Hyperfine Interact.* **113**, 493 (1998).
- ¹⁶ A.A. Vaipolin, S.A. Kijaev, L.V. Kradinova, A.M. Polubotko, V. V. Popov, V.D. Prochukhan, Y. V. Rud, and V.E. Skoriukin, *J. Phys. Condens. Matter* **4**, 8035 (1992).
- ¹⁷ F.N. Abdullaev, T.G. Kerimova, G.D. Sultanov, and N.A. Abdullaev, *Phys. Solid State* **48**, 1848 (2006).
- ¹⁸ D.A. Zocco, D.Y. Tutun, J.J. Hamlin, J.R. Jeffries, S.T. Weir, Y.K. Vohra, and M.B. Maple, *Supercond. Sci. Technol.* **25**, 084018 (2012).
- ¹⁹ J. Llanos and C. Mujica, *J. Alloys Compd.* **217**, 250 (1995).
- ²⁰ A.B. Karki, V.O. Garlea, R. Custelcean, S. Stadler, E.W. Plummer, and R. Jin, *Proc. Natl. Acad. Sci.* **110**, 9283 (2013).
- ²¹ C. Fang, B. Andrei Bernevig, and J. Hu, *Europhys. Lett.* **86**, 67005 (2009).
- ²² F. Ma, W. Ji, J. Hu, Z.-Y. Lu, and T. Xiang, *Phys. Rev. Lett.* **102**, 177003 (2009).
- ²³ C. Stock, E.E. Rodriguez, M.A. Green, P. Zavalij, and J.A. Rodriguez-rivera, *Phys. Rev. B* **84**, 045124 (2011).
- ²⁴ S. Chadov, D. Schärff, G.H. Fecher, C. Felser, L. Zhang, and D.J. Singh, *Phys. Rev. B* **81**, 104523 (2010).
- ²⁵ D.M. Basko, I.L. Aleiner, and B.L. Altshuler, in *Probl. Condens. Matter Phys.* (Oxford University Press, Oxford ; New York, 2008).
- ²⁶ T.-W. Huang, T.-K. Chen, K.-W. Yeh, C.-T. Ke, C.L. Chen, Y.-L. Huang, F.-C. Hsu, M.-K. Wu, P.M. Wu, M. Avdeev, and A.J. Studer, *Phys. Rev. B* **82**, 104502 (2010).
- ²⁷ J. Wen, S. Li, Z. Xu, C. Zhang, M. Matsuda, O. Sobolev, J.T. Park, A.D. Christianson, E. Bourret-Courchesne, Q. Li, G. Gu, D.-H. Lee, J.M. Tranquada, G. Xu, and R.J. Birgeneau, *Phys. Rev. B* **88**, 144509 (2013).
- ²⁸ N. Mott, *J. Solid State Chem.* **88**, 5 (1990).
- ²⁹ T. Kasuya, A. Yanase, and T. Takeda, *Solid State Commun.* **8**, 1551 (1970).
- ³⁰ J. Wen, G. Xu, G. Gu, J.M. Tranquada, and R.J. Birgeneau, *Reports Prog. Phys.* **74**, 124503 (2011).
- ³¹ B.C. Sales, A.S. Sefat, M.A. McGuire, R.Y. Jin, D. Mandrus, and Y. Mozharivskyj, *Phys. Rev. B* **79**, 094521 (2009).
- ³² B.H. Toby, *J. Appl. Crystallogr.* **34**, 210 (2001).
- ³³ J.H. Chu, (*Private Communication*) (2013).
- ³⁴ A. Martinelli, A. Palenzona, M. Tropeano, C. Ferdeghini, M. Putti, M.R. Cimberle, T.D. Nguyen, M. Affronte, and C. Ritter, *Phys. Rev. B* **81**, 094115 (2010).
- ³⁵ R.V. Baranova and Z.G. Pinsker, *Sov. Phys. Crystallogr.* **14**, 214 (1969).
- ³⁶ R.T. Downs and M. Hall-Wallace, *Am. Mineral.* **88**, 247 (2003).
- ³⁷ S. Nagata, P.H. Keesom, and H.R. Harrison, *Phys. Rev. B* **19**, 1633 (1979).
- ³⁸ S. Fishman and A. Aharony, *J. Phys. C Solid State Phys* **12**, L729 (1979).
- ³⁹ Y. Mizuguchi, K. Hamada, K. Goto, H. Takatsu, H. Kadowaki, and O. Miura, *Solid State Commun.* **152**, 1047 (2012).
- ⁴⁰ A. Kreyssig, M.G. Kim, S. Nandi, D.K. Pratt, W. Tian, J.L. Zarestky, N. Ni, A. Thaler, S.L. Bud'ko, P.C. Canfield, R.J. McQueeney, and A.I. Goldman, *Phys. Rev. B* **81**, 134512 (2010).
- ⁴¹ X. Lu, J.T. Park, R. Zhang, H. Luo, A.H. Nevidomskyy, Q. Si, and P. Dai, *Science* (80-.). **345**, 657 (2014).
- ⁴² D.S. Fisher, G.M. Grinstein, and A. Khurana, *Phys. Today* **41**, 56 (1988).
- ⁴³ D.P. Belanger, S.M. Rezende, A.R. King, and V. Jaccarino, *J. Appl. Phys.* **57**, 3294 (1985).
- ⁴⁴ R.J. Birgeneau, *J. Magn. Magn. Mater.* **177-181**, 1 (1998).
- ⁴⁵ M.H. Fang, H.M. Pham, B. Qian, T.J. Liu, E.K. Vehstedt, Y. Liu, L. Spinu, and Z.Q. Mao, *Phys. Rev. B* **78**, 224503 (2008).
- ⁴⁶ T. Helm and P.N. Valdivia, Unpublished (2015).
- ⁴⁷ S. Rößler, D. Cherian, H.S. Nair, H.L. Bhat, S. Elizebeth, and S. Wirth, *J. Phys. Conf. Ser.* **400**, 022099 (2012).
- ⁴⁸ S.M. Sze and K.K. Ng, *Physics of Semiconductor Devices, 3rd Edition* by S. M. Sze and Kwok K. Ng Copyright © John Wiley & Sons, Inc. (John Wiley and Sons, Inc., College Park, MD, 2007).
- ⁴⁹ S. Groves and W. Paul, *Phys. Rev. Lett.* **11**, 194 (1963).
- ⁵⁰ R. Pietrzkowski, S. Porowski, Z. Dziuba, J. Ginter, W. Giritat, and W. Sosnowski, *Phys. Stat. Sol.* **8**, K135 (1965).
- ⁵¹ N.F. Mott, *Philos. Mag.* **32**, 159 (1975).